

Photoelectrochemical biosensor with single atom sites for norepinephrine sensing and brain region synergy in epilepsy

Received: 27 November 2024

Accepted: 16 May 2025

Published online: 22 May 2025

 Check for updatesShiting Gu, Dawei Xu, Jing Huang, Xue Zhou, Yibin Liu & Zhonghai Zhang 

Norepinephrine (NE), a pivotal neurotransmitter in the central and sympathetic nervous systems, is crucial for numerous physiological and pathophysiological processes. Distinguishing NE from structurally similar dopamine and epinephrine in complex *in vivo* environments is a significant challenge. Herein, we propose a molecular docking strategy for selective, sensitive, and ultrafast detection of NE *in vivo*. Leveraging the molecular structure of NE, we design a Zn single-atom-modified TiO₂ substrate (Zn₁/TiO₂) as a photoelectrochemical (PEC) biosensor, providing synergistic atomic anchoring sites to “lock” NE molecules and enabling real-time NE detection in the brain of living male mice with a response time of 60 ms. The high specificity and rapid detection capabilities of this biosensor have unveiled a regulatory mechanism of the noradrenergic system across multiple brain regions, including the locus coeruleus, cortex, and hippocampus, highlighting a synergistic effect during epilepsy. This rationally designed single-atomic PEC biosensor for *in situ* monitoring of neurotransmitter dynamics holds promise for future brain science research.

Neurotransmitters, the vocabulary of neuronal communication, serve as the medium for cellular dialogue within the central nervous system¹. These endogenous chemical messengers precisely regulate a broad spectrum of physiological functions, including arousal, learning, and memory, emotions, and complex behaviors^{2–4}. Dysfunctional neurotransmitter signaling is often indicative of neurodegenerative and psychiatric disorders, such as epilepsy, Parkinson’s disease, and Alzheimer’s disease^{5,6}. Among neurotransmitters, the catecholamines—norepinephrine (NE), dopamine (DA) and epinephrine (EP) are particularly crucial (Fig. 1a). In the brain, distinct catecholamines mediate physiological and cognitive functions, such as movement, circulation, and reward, through specific monoaminergic pathways^{7–9}. Despite their structural similarities, these catecholamines are prone to rapid enzymatic interconversions. In the brain, NE is synthesized from DA by dopamine β-hydroxylase (DBH) in the locus coeruleus (LC), and then converted to EP by phenylethanolamine N-methyltransferase (PNMT)^{10–12}. The NE neurons, primarily originating in the LC and other brainstem nuclei, project axons throughout the central nervous system, reaching the cortex (Cx), hippocampus (Hip), hypothalamus,

amygdala, cerebellum, and spinal cord^{13–15}. Selective and swift identification of NE among its chemical analogues in the complex *in vivo* brain environment is essential for elucidating its unique neurophysiological roles. However, technical challenges have often limited traditional NE detection methods in their *in vivo* applications^{16–24}. Therefore, a method capable of reliably and ultrafast discrimination of NE from its structural analogues across different brain regions could significantly enhance our understanding of NE’s intrinsic processing and reveal the mechanisms underlying perception and behavior.

Photoelectrochemical (PEC) biosensors are an emerging class of sensing devices that utilize light as an excitation source to generate an internal electric field at the photoelectrode-electrolyte interface. This feature allows PEC biosensors to effectively avoid the stimulation on living neurons by external bias voltage, a significant advantage over traditional methods^{25,26}. However, the majority of PEC biosensors still rely on biometric probes for molecule identification, which limits their effectiveness for rapid and long-term *in vivo* molecular detection. Recently, the field of heterogeneous chemistry has seen a surge in interest in single-atom materials, offering opportunities for the precise

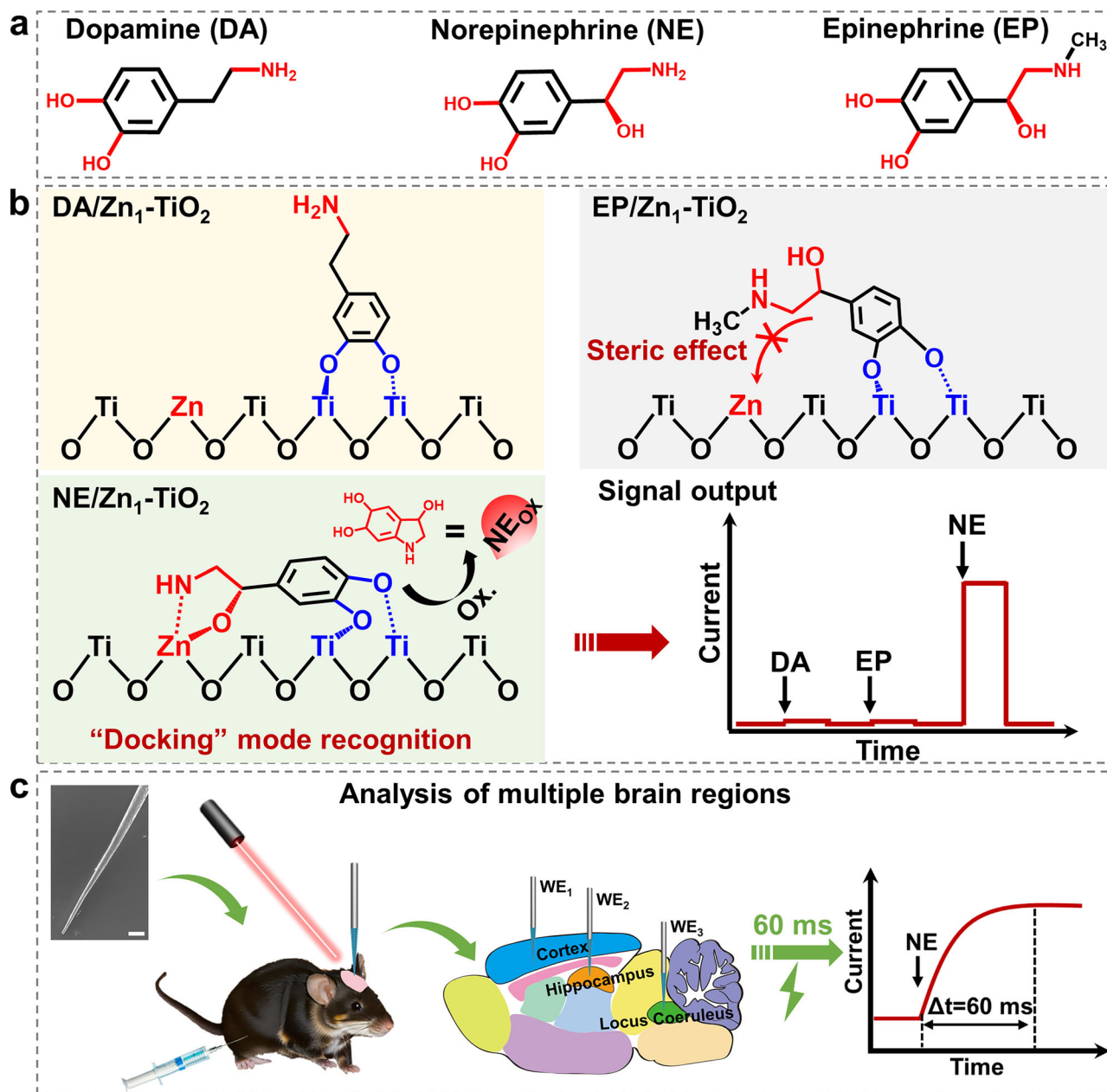


Fig. 1 | Proposed Zn₁-TiO₂ PEC biosensor for selective NE in vivo detection.

a Chemical structure formula for the three catecholamines NE, DA, and EP;

b schematic mechanism of different binding mechanisms of NE, DA and EP molecule on Zn₁-TiO₂ photoelectrode and selective photocurrent signal output of NE on

Zn₁-TiO₂ photoelectrode, the chemical structure formula of NE_{ox} represents the final reaction product of NE; **c** illustration of in vivo PEC monitoring NE in Cx, Hip, and LC with short response time of 60 ms, and the left inset shows SEM image of Zn₁-TiO₂ micro-photoelectrode (scale bar, 100 μm).

regulation of the coordination environment between single atoms and substrates²⁷. This advancement enables the reverse design of customized adsorption sites tailored for specific target molecules, potentially revolutionizing the sensitivity and specificity of PEC biosensors for in vivo applications.

Here, we introduce a PEC biosensor based on Zn single atoms on a TiO₂ substrate (Zn₁-TiO₂) for selective NE in vivo detection of NE. Figure 1b illustrates the synergistic three-site molecule recognition mechanism of NE on Zn₁-TiO₂, where NE's o-phenol hydroxyls coordinate with two adjacent Ti sites, and its hydroxyl group and primary amine group on the side-chain bond to Zn single atoms, forming a stable five-membered ring structure. The tripartite interaction creates a “lock-and-key” binding mode, enabling the Zn₁-TiO₂ photoelectrode to tightly adsorb target NE molecules at synergistic atomic anchoring

sites. Photogenerated holes subsequently oxidize NE to form NE_{ox}, which detaches from the Zn₁-TiO₂ surface (Supplementary Video 1). Unlike NE, DA and EP lack the dual recognition sites and are hindered by the steric effect of EP's methyl group, preventing unique capture by Zn₁-TiO₂. Thus, the Zn₁-TiO₂ photoelectrode can selectively detect NE by accurately distinguishing it from DA and EP. The biocompatibility of TiO₂ and the stable coordination environment of zinc single atoms ensure the biosensor's stability for long-term in vivo detection. Additionally, we engineer the Ti wire (tip diameter ~10 μm) specifically for brain implantation. To explore the relationship between NE regulation and related diseases, we establish an epileptic mouse model (Fig. 1c). We track the dynamic changes of NE in real time across LC, Cx, and Hip regions. This rationally designed PEC in vivo biosensor offers a platform for in situ monitoring of neurotransmitter dynamics, holding

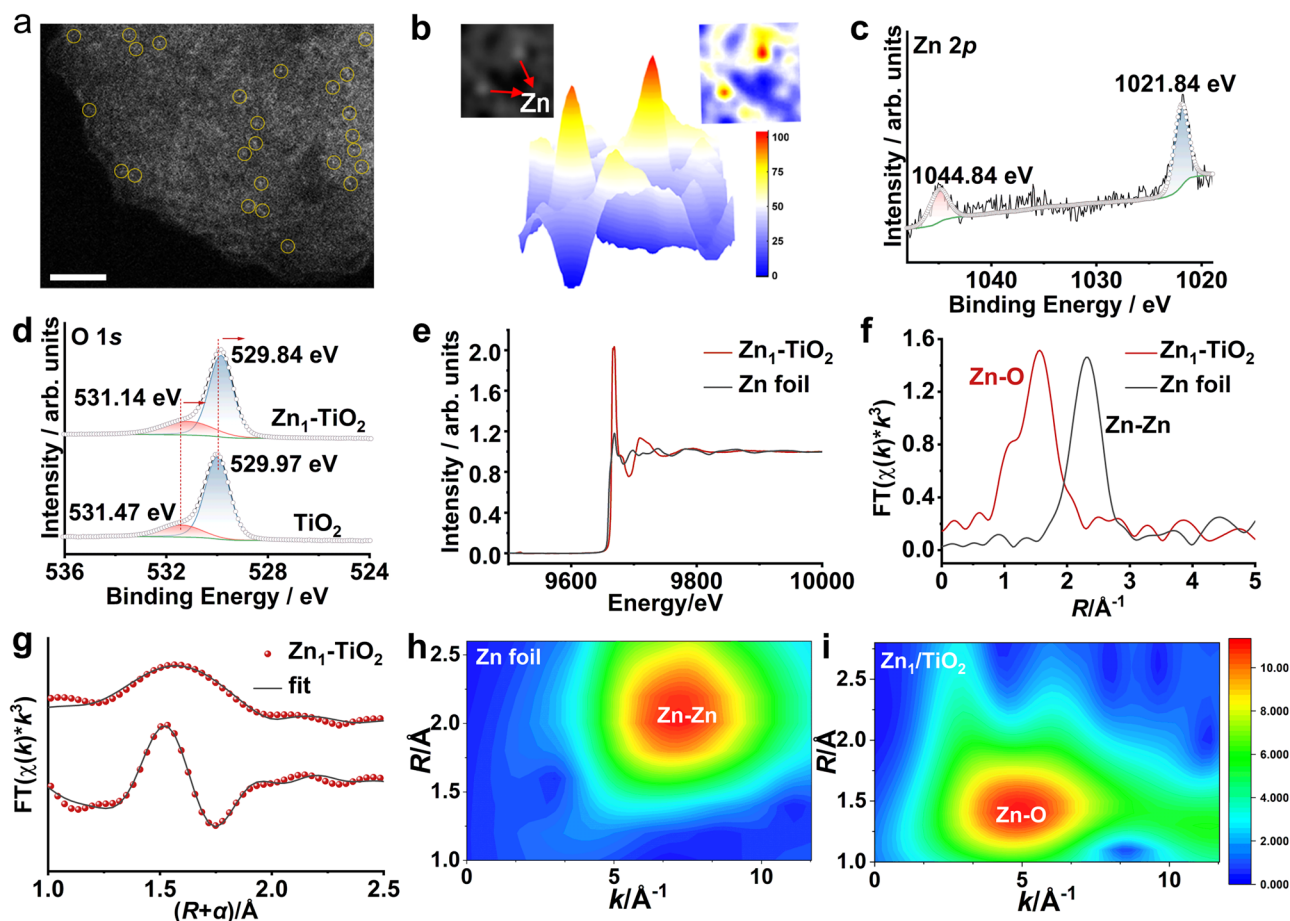


Fig. 2 | Characterizations of $\text{Zn}_1\text{-TiO}_2$. **a** Aberration-corrected high-angle annular dark-field (AC HAADF-STEM) image of $\text{Zn}_1\text{-TiO}_2$, the scale bar is 2 nm; this image is representative of at least three independent experiments with similar results; **b** 3D heatmap of the brightness of enlarged AC HAADF STEM image of $\text{Zn}_1\text{-TiO}_2$; **c** high-resolution Zn 2p XPS spectra of $\text{Zn}_1\text{-TiO}_2$; **d** high-resolution O 1s XPS spectra of TiO_2 and $\text{Zn}_1\text{-TiO}_2$; **e** Zn K-edge of near-edge XANES spectra for $\text{Zn}_1\text{-TiO}_2$ and Zn foil; **f** k^3 -weighted FT-EXAFS spectra; **g** FT-EXAFS fitting curves of Zn K-edge; wavelet transform of the k^3 -weighted EXAFS contour plots of **h** Zn foil and **i** $\text{Zn}_1\text{-TiO}_2$.

promise for neurologists and biologists to unravel the regulatory mechanism of NE in the nervous system.

Results

Fabrication and characterization of $\text{Zn}_1\text{-TiO}_2$ photoelectrode

The fabrication process of the $\text{Zn}_1\text{-TiO}_2$ photoelectrode is illustrated in Supplementary Fig. 1. A thin titanium (Ti) wire served as the electrode precursor, and TiO_2 nanotubes (TiO_2 NTs) with uniform nanotube morphology were synthesized using a two-step anodization method as previously reported²⁸. Subsequently, Zn single atoms were deposited onto TiO_2 NTs via a cryo-electrochemical deposition method. The morphology and structure of the $\text{Zn}_1\text{-TiO}_2$ NTs electrodes were characterized using scanning electron microscopy (SEM) (Supplementary Fig. 2). High-resolution transmission electron microscopy (HRTEM) revealed a clear lattice structure with a spacing distance of 0.35 nm, corresponding to the (101) plane of anatase (Supplementary Fig. 3)²⁹, which was corroborated by X-ray diffraction (XRD) results (Supplementary Fig. 4). Energy dispersive spectroscopy (EDS) mapping, inset in Supplementary Fig. 3, demonstrated the uniform distribution of Zn element across the TiO_2 NTs' surface. Inductively coupled plasma atomic emission spectroscopy (ICP-AES) confirmed the presence of Zn and showed a linear relationship between Zn content and the charge accumulated during cryo-electrodeposition (Supplementary Fig. 5). Aberration-corrected high-angle annular dark-field scanning transmission electron microscope (AC HAADF-STEM) was utilized to visualize the distribution of Zn atoms on TiO_2 NTs. Isolated bright spots in the AC HAADF-STEM

image (Fig. 2a) confirmed the presence of atomic-level Zn atoms. The 3D heatmap of the AC HAADF STEM image brightness (Fig. 2b) further indicated isolated atoms with different brightness from the TiO_2 substrate, with no Zn crystal diffraction peaks detected (Supplementary Fig. 4). The state of Zn was characterized by X-ray photoelectron spectroscopy (XPS). The core-level XPS of Zn 2p (Fig. 2c) showed peaks at 1021.84 eV and 1044.84 eV, indicative of Zn^{2+} oxidation state³⁰. Additionally, the core-level XPS of O 1s for both TiO_2 and $\text{Zn}_1\text{-TiO}_2$ was measured (Fig. 2d). The introduction of Zn single atom resulted in a negative shift of O 1s toward lower binding energy, suggesting the formation of Zn-O-Ti bonds and implying electron donation from Zn atoms to O atoms of TiO_2 .

To probe the specific atomic structure of $\text{Zn}_1\text{-TiO}_2$, X-ray absorption near-edge structure (XANES) and extended X-ray absorption fine structure (EXAFS) analyses were conducted. The XANES Zn K-edge spectra in Fig. 2e revealed higher white line intensity for $\text{Zn}_1\text{-TiO}_2$ compared to Zn foil, consistent with XPS findings indicating a high valence state of Zn in $\text{Zn}_1\text{-TiO}_2$. The Fourier-transformed (FT) k^3 -weighted EXAFS (FT-EXAFS) spectra in Fig. 2f displayed a predominant peak at 1.56 Å, assignable to the Zn-O coordination. The well-fitted curve confirmed that Zn was coordinated with five oxygen atoms (Fig. 2g and Supplementary Table S1). The absence of the Zn-Zn peak at around 2.3 Å further confirmed the atomical dispersion and oxygen stabilization of Zn atoms. Wavelet transforms contour plots of $\text{Zn}_1\text{-TiO}_2$ in Fig. 2i highlighted a Zn-O coordination peak at 4.8 Å, distinct from the Zn-Zn pair peak at approximately 7.2 Å in Zn foil (Fig. 2h, i). These results robustly

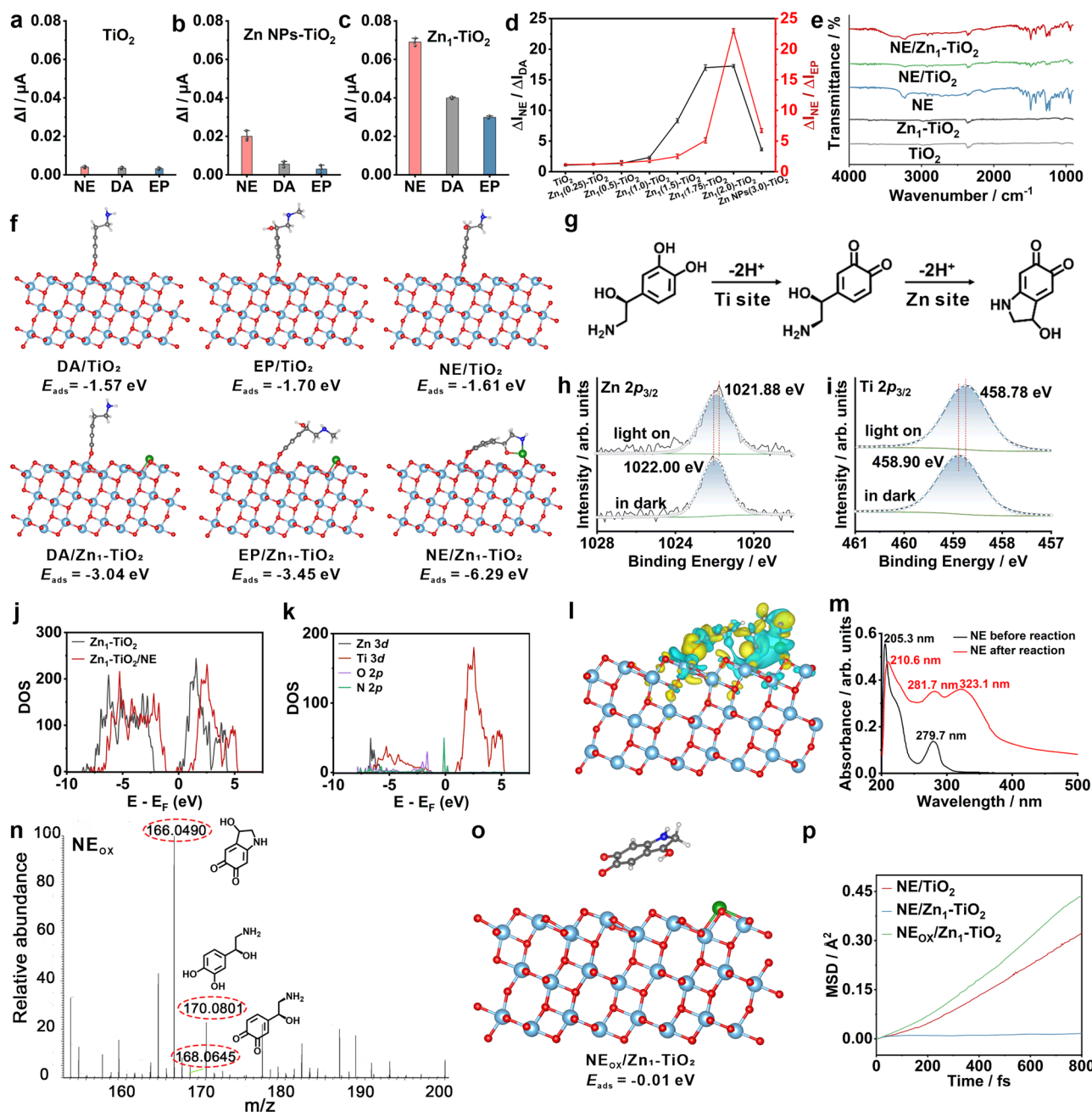


Fig. 3 | Selective PEC detection of NE. Selective PEC response of NE, DA, and EP on **a** pristine TiO_2 , **b** $Zn\ NPs-TiO_2$, and **c** Zn_1-TiO_2 ($n = 3$ electrodes), data are expressed as mean \pm SD; **d** photocurrent response ratios of NE/DA and NE/EP on TiO_2 , $Zn\ NPs-TiO_2$ and Zn_1-TiO_2 with different Zn single-atom content ($n = 3$ electrodes), data are expressed as mean \pm SD; **e** FTIR spectra of TiO_2 , Zn_1-TiO_2 , NE, NE/TiO_2 , and NE/Zn_1-TiO_2 ; **f** DFT calculations of adsorption energy of NE, DA, and EP on TiO_2 and Zn_1-TiO_2 ; **g** PEC oxidation processes of NE on Zn_1-TiO_2 ; high-resolution XPS spectra; **h** $Zn\ 2p_{3/2}$ and **i** $Ti\ 2p_{3/2}$ on NE/Zn_1-TiO_2 before and after light irradiation; **j** Total

density of states of Zn_1-TiO_2 , and NE/Zn_1-TiO_2 ; **k** partial density of states of $Zn\ 3d$, $Ti\ 3d$, $O\ 2p$ and $N\ 2p$ orbitals; **l** DFT calculations of local charge density difference of NE/Zn_1-TiO_2 , yellow part symbolizes local electron accumulation area and cyan part symbolizes local electron depletion area respectively; **m** UV-visible absorption spectra of NE before and after PEC oxidation; **n** LC-MS spectra of NE after PEC oxidation on Zn_1-TiO_2 ; **o** DFT calculations of adsorption energy of NE_{ox} on Zn_1-TiO_2 ; **p** MSD diagrams of NE on TiO_2 , NE on Zn_1-TiO_2 and NE_{ox} on Zn_1-TiO_2 .

validate the feasibility of modifying TiO_2 with Zn_1 to fabricate the Zn_1-TiO_2 photoelectrode.

Selective PEC response of NE on Zn_1-TiO_2 photoelectrode

The rationally designed Zn_1-TiO_2 photoelectrodes were employed for the selective PEC detection of NE. The selectivity for NE, DA, and EP was compared on pristine TiO_2 , Zn nanoparticles- TiO_2 ($Zn\ NPs-TiO_2$), and Zn_1-TiO_2 . As shown in Fig. 3a, pristine TiO_2 exhibited weak and similar photocurrent responses to NE, DA, and EP at 20 nM concentrations,

indicating no selectivity for NE detection. In contrast, $Zn\ NPs-TiO_2$ (Fig. 3b) showed a modest increase in photocurrent response for NE, attributed to the limited number of anchoring sites for NE molecules. However, Zn_1-TiO_2 (Fig. 3c) demonstrated a significantly higher photocurrent change for NE compared to DA and EP, even when the concentrations of DA and EP were 50 times higher than that of NE (Supplementary Fig. 6), which highlights its excellent selectivity for NE. This selectivity was also observed for the non-catecholamine neurotransmitter serotonin (5-HT), metabolite of NE (DOPET and DOPEGAL),

as well as some possible interfering substances (Supplementary Figs. 7–9) and in artificial cerebrospinal fluid (aCSF) (Supplementary Fig. 10), underscoring the potential for selective NE recognition under complex in vivo conditions.

The selectivity ratios of NE over DA and EP for different samples are summarized in Fig. 3d. $\text{Zn}_1(2.0)\text{-TiO}_2$, with a 2.0 % weight ratio of Zn single atom on TiO_2 , exhibited the highest selectivity and was used in subsequent experiments unless specified otherwise. Additionally, the incorporation of Zn single atoms into TiO_2 was found to enhance the photoelectric conversion efficiency and electron transport rate of the photoelectrode, as characterized by PEC performance (Supplementary Fig. 11) and electronic structure variations (Supplementary Figs. 12, 13). This modification also narrowed the band gap and improved optical absorption (Supplementary Fig. 14), consistent with the band structure and density of states (Supplementary Fig. 15).

To provide direct experimental evidence of NE molecular adsorption on $\text{Zn}_1\text{-TiO}_2$, Fourier transform infrared (FTIR) spectra were measured. Figure 3e shows that NE molecules exhibit multiple absorption peaks between 1000 and 1700 cm^{-1} , attributed to the characteristic stretching vibration of C–H in the aromatic ring and C–N on the side chain, and a broad peak at ~3300 cm^{-1} due to the stretching vibration of the hydroxyl group³¹. Upon introduction of NE, the FTIR spectrum of $\text{NE/Zn}_1\text{-TiO}_2$ exhibited significantly enhanced and distinct absorption peaks compared to that of NE/TiO_2 , particularly in the 1000–1700 cm^{-1} region (aromatic C–H and C–N stretching) and near 3300 cm^{-1} (O–H stretching). These features suggest stronger and more specific interactions between NE and $\text{Zn}_1\text{-TiO}_2$, consistent with the proposed coordination between NE's o-phenol hydroxyl groups and adjacent Ti sites, as well as its side-chain hydroxyl and amine groups with Zn single atoms. In contrast, the NE/TiO_2 spectrum showed only weak adsorption signals. Furthermore, FTIR spectra of DA and EP on $\text{Zn}_1\text{-TiO}_2$ (Supplementary Fig. 16) revealed negligible peak shifts, supporting the high selectivity of $\text{Zn}_1\text{-TiO}_2$ for NE through a unique molecular recognition mechanism.

To elucidate the high selectivity of NE on $\text{Zn}_1\text{-TiO}_2$, density function theory (DFT) calculations were performed using DS-PAW software³². The adsorption status and energies of NE, DA, and EP on TiO_2 and $\text{Zn}_1\text{-TiO}_2$ are shown in Fig. 3f. On pristine TiO_2 , NE, DA, and EP showed similar adsorption energies, indicating a common binding mode with o-phenol hydroxyl coordinating with two adjacent Ti sites. On $\text{Zn}_1\text{-TiO}_2$, DA and EP maintained this binding with slightly increased adsorption energies, suggesting that Zn single atoms did not significantly alter their adsorption. However, NE on $\text{Zn}_1\text{-TiO}_2$ formed a new five-membered ring structure with Zn single atoms, significantly increasing its adsorption energy. This unique interaction firmly locked NE molecules onto $\text{Zn}_1\text{-TiO}_2$, explaining the observed selectivity.

Under PEC condition, the potential oxidation routes of NE on $\text{Zn}_1\text{-TiO}_2$ were proposed (Fig. 3g). The o-phenol hydroxyl would oxidize to quinone, and the primary amine to secondary amine. The oxidation product NE_{ox} would not remain on the $\text{Zn}_1\text{-TiO}_2$ surface, which was favorable for continuous long-term in vivo NE detection. Synchronous illumination X-ray photoelectron spectroscopy (SI-XPS) provided experimental evidence of the interaction between NE and $\text{Zn}_1\text{-TiO}_2$ (Fig. 3h, i). The core-level XPS spectra revealed distinct differences between $\text{Zn}_1\text{-TiO}_2$ and $\text{NE/Zn}_1\text{-TiO}_2$, further confirming the specific adsorption of NE on the photoelectrode surface. Upon NE adsorption, the Zn $2p_{3/2}$ and Ti $2p_{3/2}$ peaks exhibited noticeable negative shifts in binding energy under illumination, suggesting that photogenerated holes were effectively transferred from the Zn and Ti sites to the NE molecules. This shift indicates strong electronic interaction and charge transfer involved in the NE anchoring process. In contrast, the O 1s spectra displayed negligible changes in binding energy between dark and illuminated conditions, implying that oxygen atoms on the TiO_2 substrate were not the primary participants in the interfacial charge transfer (Supplementary Fig. 17). These XPS results support the dual-

site coordination mechanism proposed for NE, in which both Ti and Zn centers serve as active anchoring and charge transfer sites.

The total densities of states (TDOS) of $\text{Zn}_1\text{-TiO}_2$ before and after NE absorption were calculated (Fig. 3j). The TDOS shifted slightly to the right after NE absorption, with new peaks appearing near the Fermi level, possibly due to orbital hybridization between NE and photoelectrode surface atoms. The partial densities of states (PDOS) of $\text{NE/Zn}_1\text{-TiO}_2$ (Fig. 3k) showed significant orbital hybridization between N/O atoms and Ti/Zn atoms at -1.95 eV and -6.5 eV. These results suggest strong orbital interactions between NE with $\text{Zn}_1\text{-TiO}_2$, leading to large charge transfer and stable absorption. To further investigate the interaction, the spatial charge redistribution on the interface was calculated (Fig. 3l). Strong charge transfer activity between NE and $\text{Zn}_1\text{-TiO}_2$ was observed, with charge accumulation in Ti and Zn sites and depletion in the o-phenol hydroxyl oxygen and hydroxyl and amino groups on the NE side chain. This demonstrates that Zn and Ti sites on $\text{Zn}_1\text{-TiO}_2$ function as “lock” to capture NE and as charge channels to oxidize it.

The UV-vis absorption spectra of NE solution were measured before and after PEC oxidation to preliminarily identify NE oxidation products. Figure 3m shows that a new absorption peak at 323.1 nm emerged after the PEC reaction, indicative of a new five-membered ring structure formation³³. Liquid chromatograph-mass spectrometer (LC-MS) was then employed to elucidate the structure of the NE oxidation products. The dominated m/z peak at 170.0800, corresponding to the original NE molecule, decreased in intensity after PEC oxidation (Supplementary Fig. 18). Concurrently, a new dominant m/z peak at 166.0490 appeared, which can be attributed to the final product of NE_{ox} (Fig. 3n). Furthermore, a linear PEC response of NE on $\text{Zn}_1\text{-TiO}_2$ was observed in the range of 10 nM to 3.5 μM , with a limit of detection (LOD, S/N=3) of 3.1 nM (Supplementary Fig. 19). This LOD is significantly lower than the reported concentration of NE in cerebrospinal fluid³⁴, indicating that our sensor is sufficiently sensitive for in vivo NE detection and suitable for monitoring neurotransmitter levels in brain regions. Additionally, the response time of the NE on the $\text{Zn}_1\text{-TiO}_2$ photoelectrode is 60 ms (Supplementary Fig. 20), ensuring the potential for rapid in vivo monitoring of dynamic fluctuations in NE concentration in the brain. The sensor's 60 ms response time reflects the PEC system's signal stabilization, distinct from the sub-picosecond NE/ NE_{ox} adsorption/desorption dynamics. Additionally, different from conventional fluorescent molecules rely on conformational changes, which introduce delays due to molecular rearrangements, in contrast, PEC detection directly converts molecular binding events into electronic signals via interfacial charge transfer, bypassing slow structural transitions.

DFT calculations were performed to assess the interaction between the oxidation product of NE, NE_{ox} , and $\text{Zn}_1\text{-TiO}_2$. Figure 3o shows an adsorption energy of -0.01 eV for the $\text{NE}_{\text{ox}}/\text{Zn}_1\text{-TiO}_2$ system, significantly higher than that of the $\text{NE/Zn}_1\text{-TiO}_2$ system (-6.29 eV), indicating that NE_{ox} has a lower affinity for the $\text{Zn}_1\text{-TiO}_2$ surface. To visualize the migration of NE and NE_{ox} on the photoelectrode surface, mean square displacement (MSD) calculations were conducted. The MSD is defined by the formula (1):

$$\text{MSD} = \frac{1}{N} \sum_{i=1}^N \langle |r_i(0) - r_i(t)|^2 \rangle \quad (1)$$

where $r_i(0)$ is the initial position of atom i , and $r_i(t)$ is the position of atom i after time t , and the brackets $\langle \rangle$ denote the average square of the displacement. N is the total number of molecules in the MSD calculation. The MSD, which represents the square of the displacement of the molecule per unit time, is plotted in Fig. 3p for NE and NE_{ox} diffusing on different photoelectrode materials. The steeper the MSD curve, the higher the molecular mobility. Figure 3p reveals that the mobility order of NE or NE_{ox} on the photoelectrode surface is

$\text{NE}_{\text{OX}}/\text{Zn}_1\text{-TiO}_2 > \text{NE}/\text{TiO}_2 > \text{NE}/\text{Zn}_1\text{-TiO}_2$. This suggests that NE is more readily adsorbed on $\text{Zn}_1\text{-TiO}_2$ than on TiO_2 , and NE_{OX} is less likely to adsorb on $\text{Zn}_1\text{-TiO}_2$, aligning with the adsorption energy calculations. Energy changes in the NE/TiO_2 , $\text{NE}/\text{Zn}_1\text{-TiO}_2$, and $\text{NE}_{\text{OX}}/\text{Zn}_1\text{-TiO}_2$ systems during molecular dynamics simulations further confirm the stability of NE adsorption on $\text{Zn}_1\text{-TiO}_2$ (Supplementary Fig. 21). Consequently, our $\text{Zn}_1\text{-TiO}_2$ photoelectrode not only exhibits excellent NE adsorption performance but also demonstrates reusability (Supplementary Fig. 22).

PEC in vivo detection of NE

Prior to in vivo NE detection using the implanted $\text{Zn}_1\text{-TiO}_2$ micro-photoelectrode, an anti-biofouling hydrogel layer was applied to the photoelectrode surface to prevent biological contamination from proteins, platelets, and cells^{35,36}. The anti-biofouling efficacy of the hydrogel layer was assessed through static water contact angle measurements, analysis of fluorescein isothiocyanate (FITC)-labeled protein adsorption, and electrochemical characterizations (Supplementary Figs. 23, 24). The hydrogel layer, characterized by high hydrophilicity and appropriate nanoporous structures, exhibited superior anti-biofouling properties without compromising the detection of small molecule neurotransmitters (Supplementary Fig. 25).

Leveraging its high selectivity for NE and anti-biofouling properties, the $\text{Zn}_1\text{-TiO}_2$ micro-photoelectrode was deployed for in vivo NE detection in the brain of a living mouse. NE is primarily synthesized in the LC, a nerve nucleus located in the pons^{37,38}. Thus, the $\text{Zn}_1\text{-TiO}_2$ micro-photoelectrode was stereotactically implanted into the LC (Fig. 4a) to monitor NE release triggered by pharmacological compounds. Figure 4b shows a distinct decrease in photocurrent following the administration of clonidine (0.3 mg/Kg), an α -2 NE receptor agonist that reduces central NE levels³⁹. In contrast, mice injected with atomoxetine (1 mg/Kg), a NE reuptake inhibitor (NRI)⁴⁰, exhibited a significant increase in photocurrent (Fig. 4c). Additionally, subcutaneous injection of 50 mM K^+ led to a rapid increase in photocurrent response (Fig. 4d), due to the stress-induced neuronal reaction to high K^+ concentrations, which enhances the exocytosis of noradrenergic neurons and increases NE concentration.

To validate the PEC detection results, the change of norepinephrine concentration was detected by MD-HPLC (Fig. 4e). Prior to this, we verified the selectivity and accuracy of PEC sensor by comparing the results of PEC sensor and HPLC method for measuring NE concentration in brain homogenate extract (Supplementary Figs. 26–28 and Table S2). Figure 4f shows a significant decrease in NE concentration in the cerebrospinal fluid of clonidine-treated mice. The concentration of NE in atomoxetine and high K^+ treatment was significantly higher than that in the control group, indicating that the NE released by neurons in the locus coeruleus region increased (Fig. 4g, h). These results confirm that $\text{Zn}_1\text{-TiO}_2$ micro-photoelectrode accurately reflected in vivo NE detection activity in the mouse brain.

PEC in vivo NE detection across different brain regions in epilepsy model

To elucidate the relationship between NE concentration variations in different brain regions during psychiatric disorders, an epilepsy model was induced by injecting pentylenetetrazol (PTZ). Epilepsy, a complex brain disease involving regions such as Cx and Hip, is known to be associated with the LC-NE system, which plays an anti-epileptic role during seizures⁴¹. Despite the recognized importance of NE concentration changes in epilepsy, there has been a lack of reliable methods for in situ and real-time monitoring of NE in multiple brain regions. The $\text{Zn}_1\text{-TiO}_2$ micro-photoelectrodes were thus employed to simultaneously monitor NE dynamics in the LC, Cx, and Hip during epilepsy (Fig. 5a), while EEG recordings were used to define seizure phases (Fig. 5b). The NE concentrations, linearly related to photocurrent change, were recorded across multiple brain regions (Fig. 5c),

with the photocurrent over time presented in Fig. 5d. EEG analysis revealed that at seizure onset, NE concentration in the LC rapidly increased, likely due to the massive release of NE from LC neurons, which coincided with the appearance of high-amplitude spike-wave discharges in the EEG. Concurrently, NE concentration in the Cx quickly increased, attributed to reduced GABA-mediated inhibition in cortical structures, leading to excessive excitation and synchronous abnormal neuronal discharge⁴². The LC neurons timely released NE to inhibit cortical discharge caused by epilepsy. Later in seizures, a significant decrease in photocurrent in the Hip was observed, possibly due to hippocampal-cortical coupling induced by epilepsy, inhibiting abnormal cortical discharge, and severe damage to hippocampal neurons. After mice recovered from epilepsy, photocurrent in the Cx and LC returned to normal, corresponding to the normalization of EEG activity, while the Hip's photocurrent remained altered due to neuronal damage. The close temporal correlation between EEG-defined seizure phases and NE dynamics highlights the critical role of NE in modulating epileptic activity and underscores the utility of the $\text{Zn}_1\text{-TiO}_2$ micro-photoelectrodes for real-time monitoring of neurotransmitter dynamics in vivo.

Control experiments were conducted to further understand the relationship between NE concentration variations and epilepsy development. A control group injected with saline showed no significant photocurrent fluctuations (Supplementary Fig. 29). Another group, pre-injected with the anti-epileptic drug zonisamide (ZNS) to block PTZ-induced epilepsy, also showed no photocurrent variation in all three brain regions. Consistent with this, EEG recordings confirmed the absence of epileptiform activity, such as spike-wave discharges or high-amplitude oscillations, indicating that ZNS effectively prevented seizures and stabilized neurotransmitter concentrations, indicating that ZNS prevented seizures and neurotransmitter concentration fluctuations (Fig. 5e, f). In addition, we compared the NE content in cerebrospinal fluid of mice treated with epilepsy and ZNS by HPLC, and the results showed that the NE content in LC and CX brain region of epilepsy group was significantly higher than that in ZNS group, while the NE content in hip brain region was slightly lower than that in ZNS group (Supplementary Fig. 30). Finally, a third control group, injected with insulin after a 24 h fast, showed a significant photocurrent increase due to physiological stress response (Supplementary Fig. 31). These results demonstrate that the $\text{Zn}_1\text{-TiO}_2$ micro-photoelectrode is a promising tool for monitoring NE and evaluating the therapeutic effect of NE-related diseases.

Following seizures, the extent of damage in three brain regions was assessed using immunohistochemistry and behavioral experiments. Caspase-3, a key enzyme in apoptosis⁴³, was targeted for immunohistochemical staining on brain sections to evaluate cell apoptosis before and after seizures. Figure 5g shows a significant increase in caspase-3 protein expression in the Hip post-epilepsy, while the Cx and LC exhibited no significant change, indicating severe neuronal damage in the Hip and minimal damage in the Cx and LC^{44–46}. The control group with insulin showed no change in caspase-3 protein expression (Supplementary Fig. 32).

The Hip's role in memory was further analyzed using a new object recognition (NOR) test. Figure 5h demonstrates that epileptic mice had a lower recognition rate than normal mice, suggesting that epilepsy impaired NOR memory and damaged the Hip memory function. The motor cortex, involved in movement control, was evaluated using a locomotor activity test in an open area (Fig. 5i). The total movement distance of mice after 12 h of epilepsy was similar to that of normal mice, indicating that epilepsy did not significantly affect the motor cortex function (Fig. 5j).

Discussion

In summary, we developed a $\text{Zn}_1\text{-TiO}_2$ photoelectrode featuring atomic docking unit for the selective in vivo detection of NE molecules. The

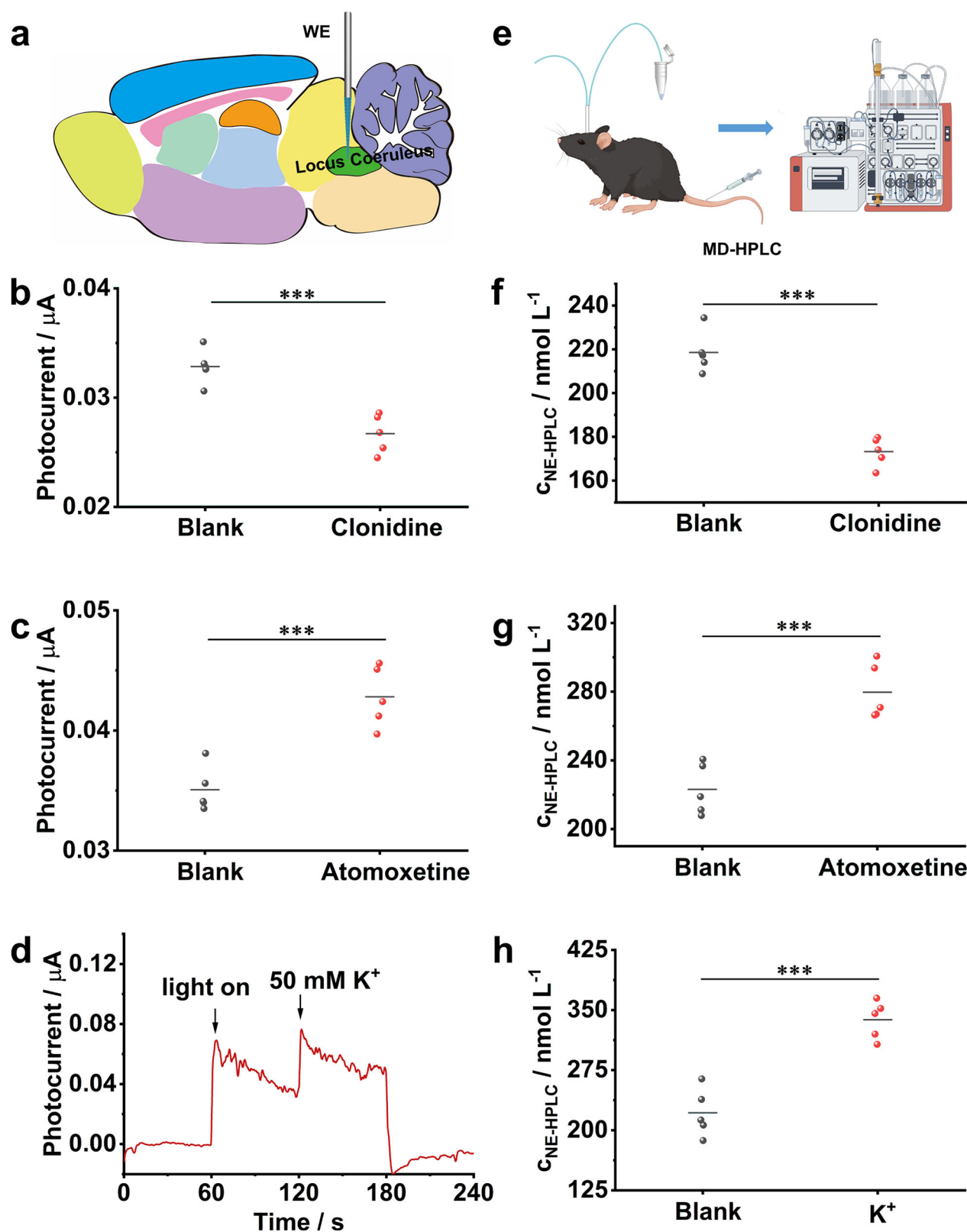


Fig. 4 | PEC in vivo NE detection in single brain region of LC. **a** Schematic of micro-photoelectrode in LC for NE measurement; photocurrent responses of implanted micro-photoelectrode in LC of mice after injection of **b** 0.3 mg/Kg clonidine ($n = 5$ mice), **c** 1.0 mg/kg atomoxetine ($n = 5$ mice), and **d** 50 mM K^+ ; **e** Schematic diagram of MD-HPLC test; NE concentration in LC region of mice

determined by MD-HPLC after injection of **f** 0.3 mg/Kg clonidine, **g** 1.0 mg/kg atomoxetine, and **h** 50 mM K^+ ($n = 5$ mice). Data are expressed as mean \pm SD. Statistical significance is calculated with two-tailed unpaired t -test and p -values are indicated (ns $p > 0.05$, * $p < 0.05$, ** $p < 0.01$, and *** $p < 0.001$).

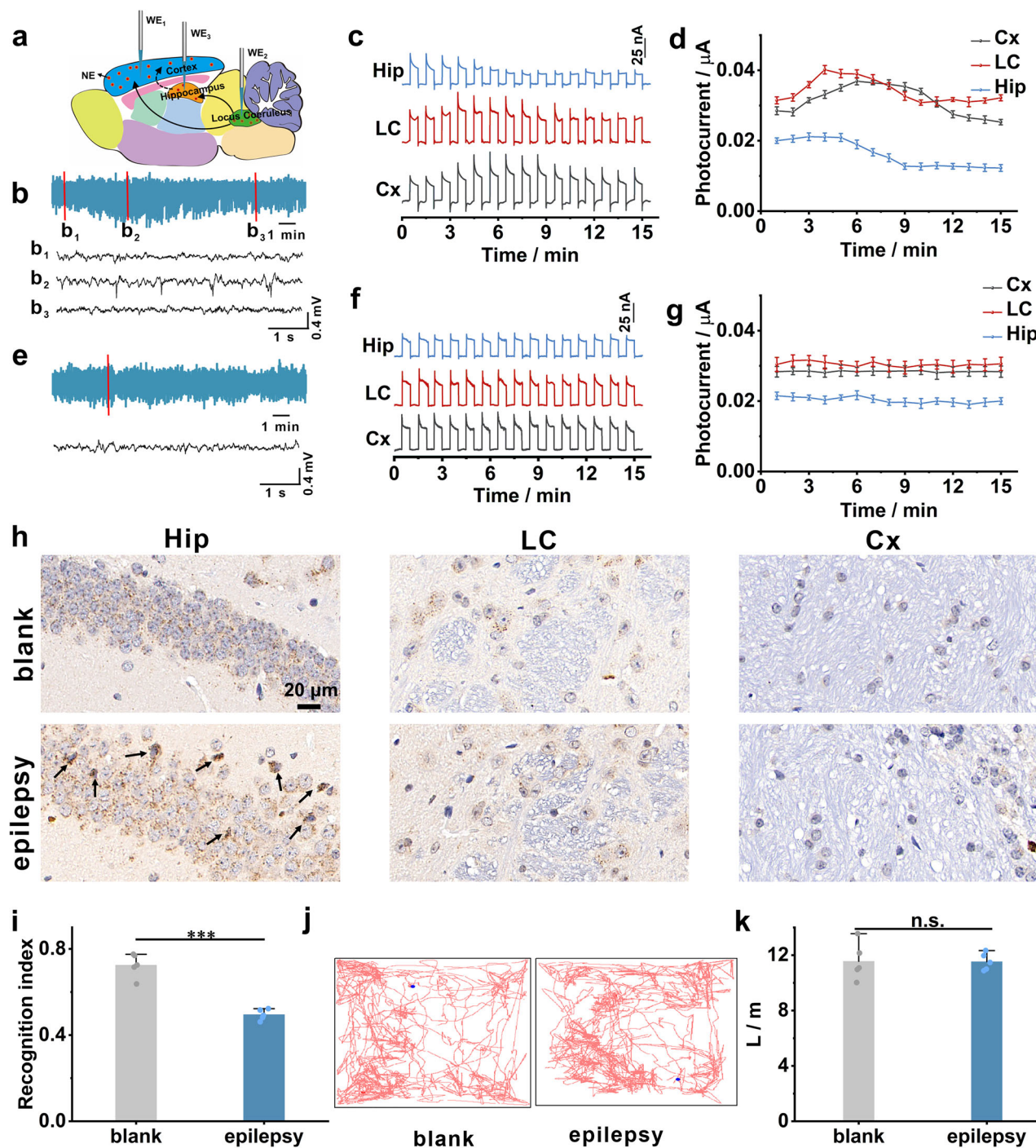


Fig. 5 | PEC in vivo NE detection in different brain regions. **a** Schematic multi-micro-photoelectrodes in Cx, LC, and Hip for simultaneous NE measurements; **b** representative EEG recordings of the Cx after injection of PTZ (65 mg/kg), and the magnified EEG images of three important stages of epilepsy. **b**₁: pre-epilepsy period, **b**₂: epilepsy period, **b**₃: post-epilepsy period; **c** photocurrent signals and **d** corresponding line charts of NE on Zn₁-TiO₂ micro-photoelectrodes in Cx, LC, and Hip of mice brain in epilepsy condition; Data are expressed as mean ± SD (***p* < 0.001). **e** Representative EEG recordings of Cx in mice treated with 2.0 mg/kg

zonisamide followed by PTZ injection; **f** photocurrent signals and **g** corresponding line charts of NE on Zn₁-TiO₂ photoelectrodes in Cx, LC, and Hip of mice brain in epilepsy condition with injection of 2.0 mg/kg zonisamide schematic multi-micro-photoelectrodes in Cx, LC, and Hip for simultaneous NE measurements; **h** caspase-3 activity in Hip, LC, and Cx in epileptic and normal mice; **i** new object recognition (NOR) ability of mice before and after epilepsy; **j** typical motion tracks of mice in 5 min in a quadrangle empty arena; **k** total distance that mice moved before and after epilepsy (*n* = 5 mice, and n.s., no significance). Data are expressed as mean ± SD.

o-phenol hydroxyls of NE coordinate with two adjacent Ti sites, while the hydroxyl and primary amine groups on the side-chain bond with Zn single atoms, forming a stable five-membered ring structure. Leveraging the selective and rapid NE recognition capabilities of Zn₁-TiO₂, we elucidated the regulatory mechanisms of NE in the LC, Cx, and Hip during the epilepsy disorder model, revealing a synergistic NE release

from the LC and Hip to inhibit abnormal discharge in the Cx. We believe that this atomic anchoring recognition strategy for target molecule detection paves the way for rationally designing selective, rapid, robust, and stable in vivo detection platforms, facilitating reliable quantitative analysis of essential molecules in complex biological systems.

Methods

Ethical statement

All animal care and in vivo procedures were conducted in accordance with the guidelines set by the Animal Care and Use Committee of East China Normal University (approval no. R20240306, Shanghai, China).

Materials and reagents

Titanium wires (0.1 mm diameter, 99.6% purity) were obtained from Jinjia Metal, China. Ethylene glycol (EG), ammonia fluoride (NH_4F), zinc sulfate (ZnSO_4), sodium chloride (NaCl), dibasic sodium phosphate (Na_2HPO_4), potassium dihydrogen phosphate (KH_2PO_4), dopamine hydrochloride (DA), norepinephrine hydrochloride (NE), Epinephrine hydrochloride (E) were purchased from Maclin Biochemical Technology Co., Ltd. (Shanghai, China).

Apparatus

The morphologies and elemental mappings of electrode materials were characterized by scanning electron microscopy (SEM, S4800, Hitachi) and high-resolution transmission electron microscopy (HR-TEM, JEOL JEM 2100). The distribution of single atom was observed by High-angle annular dark-field scanning transmission electron microscopy (HAADF-STEM, JEOL Grand ARM300). The content of Zn in the sample was determined on inductively couple plasma optical emission spectrometer (ICP-OES, Thermo Fisher, iCAP7200). XPS measurements were conducted at an Axis Ultra spectrometer (Kratos Analytical) under ultrahigh vacuum ($<10^{-8}$ Torr) and by using a monochromatic Al K α X-ray source. The diffuse reflectance UV-Vis-NIR adsorption spectra (DRS) was detected on a spectrophotometer (Shimadzu, UV 3600). The crystal structure of samples was analyzed by X-ray diffraction (XRD) [Bruker D8 Discover diffractometer, using Cu K α radiation (1.540598 Å)]. The mass spectra were detected by an ultrahigh-performance liquid chromatography couple to quadrupole high-resolution mass spectrometer (HPLC-MS, ThermoFisher, Q-Exactive). Tissue sections were performed on a pathological microtome (Shanghai Leica Instruments Co., LTD., China). Immunofluorescence images were observed and collected using a standing fluorescence microscope (Nikon Eclipse C1, Japan). Photocurrent was measured on a CHI 660E electrochemical workstation (Shanghai Chenhua Apparatus Corporation, China) with a near-infrared light lamp (applied potential: 0 V).

Preparation of $\text{Zn}_1\text{-TiO}_2$. The TiO_2 NTPCs were fabricated by a two-step anodization process according to the reported method. Prior to anodization, the titanium wires were ultrasonically cleaned in acetone, ethanol, and DI water, and then dried in a pure nitrogen stream. The anodization was performed in a traditional two-electrode system with a Ti wire as anode and a Pt foil as cathode. The electrolyte of the two-step system was 0.5 wt% NH_4F in an EG solution with 2 vol% water. First, the Ti wire was anodized at 60 V for 30 min, and then the first layer of nanotubes was removed by ultrasonic in water. Subsequently, the same titanium wire was secondary anodized at 30 V for 30 min. After washing with water, the prepared TiO_2 NTPCs were dried off with nitrogen. Finally, the TiO_2 NTPCs was annealed in air at 500 °C for 1 h. The $\text{Zn}_1\text{-TiO}_2$ NTPCs electrode was prepared by the cryoelectrochemistry method. Zinc sulfate (50 mM) dissolved in dilute sulfuric acid was used as Zn single atom precursor. Then the TiO_2 NTPCs electrode was immersed in the precursor solution for 1 h. Subsequently, the TiO_2 NTPCs electrode with 4 mL Zn precursor solution and a typical two-electrode system with Pt foils as counter electrode and working electrode were immersed in liquid nitrogen for 5 min. After that, the frozen system was put into a cold trap with a slow potentiostatic electrodeposition at -10 V, and the amount of charge applied was recorded. After the frozen system melting at room temperature, the obtained $\text{Zn}_1\text{-TiO}_2$ electrode was washed with DI water and dried with nitrogen gas.

Modification of hydrogel. The antifouling interface of hydrogel was prepared by using diethylacrylamide and hydroxyethylacrylamide as mixed acrylamide hydrogel monomers. Hydrogel prepolymer containing 20 wt% arylamide monomer, 1 wt% lithium phenyl-2,4,6-trimethylbenzoylphosphine (LAP) as photoinitiator, and 1 wt% methylenediacrylamide was dissolved in DI water. The prefabricated hydrogel mixture was coated on the surface of $\text{Zn}_1\text{-TiO}_2$ electrode, and crosslinked under UV light to obtain Gel/ $\text{Zn}_1\text{-TiO}_2$ electrode.

Animal studies. Male C57 mice (6–8 weeks old, 18–20 g in weight) were obtained from the Animal Experimental Center of East China Normal University. The mice were housed with adequate food and water in an environment with suitable temperature and humidity and under a 12 h light/dark schedule with adequate food and water.

Drug effect. All the mice were deprived of water and food for 12 h before the experiment. The mouse was first placed in a mouse stereotaxic frame and kept anesthetized by an isoflurane gas anesthesia machine. A heating blanket was used to maintain the body temperature of mice. The location of the LC (AP = -5.4 mm, ML = 0.8 mm, DV = -3.8 mm) brain region of the mouse was accurately located through a stereotaxic instrument, and the skull was drilled by cranial drill. Then, the $\text{Zn}_1\text{-TiO}_2$ photoelectrode was implanted into the LC and fixed with dental cement. The counter electrode was implanted in the same way into the brain area two millimeters away from the working electrode. Drug-induced NE release was performed on the mouse above. First, a photocurrent was measured as blank value. Then, the mouse was intraperitoneally injected with atomoxetine (1.0 mg/kg) or clonidine (1.0 mg/kg), and K^+ (50 mM) was injected subcutaneously through the neck. Photocurrent signal acquisition was performed again 30 min after drug injection.

NE sensing in three brain regions in epilepsy mouse. The experimental mouse of epilepsy (EP) was induced by injecting with pentylenetetrazole (PTZ) (65 mg/kg) intraperitoneally. Then, the behavior of mice was observed. Seizures induced were divided into six behavior categories (grade 0–5): grade 0: normal non-epileptic activity, grade 1: snout and facial movements, hyperactivity, grooming, sniffing, scratching, and shakes. Grade 2: head nodding, staring, and tremor. Grade 3: forelimb clonus and forelimb extension. score 4: rearing and salivating. Grade: falling and status epilepticus. And mice were randomly assigned to different groups. The mice in the control group were injected with the same volume of normal saline.

The anesthetized EP mice were fixed on a stereotaxic frame. According to standard stereotaxic procedures, the photoelectrodes were implanted into different mice brain areas and affixed to the skull using dental cement. The coordinates of cortex (Cx), hippocampus (hip), locus coeruleus (LC) are (AP = 0.8 mm, ML = -1.0 mm, DV = -1.5 mm), (AP = -2.0 mm, ML = -1.5 mm, DV = -2.0 mm) and (AP = -5.4 mm, ML = 0.8 mm, DV = -3.8 mm), respectively. Before measuring, the gas anesthesia was stopped. Then, the photocurrent during the epilepsy of the mice was recorded.

Anti-epileptic drugs, zonisamide (ZNS), was used to prevent epilepsy. The fixed on a stereotaxic frame mouse was implanted photoelectrodes into three different brain area, including Cx, Hip and LC. Then, zonisamide (2 mg/kg) was intraperitoneally injected into mice. After 30 min, PTZ (65 mg/kg) was intraperitoneally injected into the mouse. The photocurrent was recorded, and it was observed whether the mice were epileptic at the same time.

The mice were randomly divided into two groups. The brains of mice in the control group were removed and fixed in paraformaldehyde (40 g/L, pH = 7.4) at 4 °C for 48 h. The mice in the experimental group were injected with PTZ (65 mg/kg) to induce epilepsy. The mice with epilepsy up to Racine scale 5 were decapitated. The brain tissue of epilepsy mice was taken out carefully and fixed in paraformaldehyde.

After being washed with water, the brain tissues were dehydrated and embedded in paraffin. Then, continuous coronal sections were made on a paraffin slicer with a thickness of 5 microns. Brain regions of the Hip, LC, and Cx were expanded in 40 °C DI water. The samples were spooned with cleaned slides coated with polylysine and dried for use. Paraffin sections were stained immunohistochemically according to the DBA kit instructions for the observation of pathological changes in different brain regions.

HPLC-ECD analysis. The concentration of norepinephrine (NE) was quantified using HPLC (Shimadzu, LC-20A) with ECD-20A detector. A C18 column (250 mm × 4.6 mm, 5 μm) was employed, with a mobile phase consisting of methanol-KH₂PO₄ (1:9, v/v, pH 6.0) delivered at a flow rate of 0.8 mL/min. The column temperature was maintained at 30 °C, and the electrochemical detector was set at a working voltage of 0.8 V.

LC-MS analysis. The analysis was performed using a quadrupole ultrahigh resolution liquid chromatography-mass spectrometry system (Thermo Fisher QE) equipped with an electrospray ionization (ESI) source operating in negative ion mode (ESI⁻). Key parameters included: negative ion spray voltage of 3.0 kV, ion transfer tube temperature of 300 °C, vaporizer temperature of 300 °C, sheath gas (N₂) flow rate of 40.9 L min⁻¹, auxiliary gas (N₂) flow rate of 5.08 L min⁻¹, and argon as collision gas. Data acquisition employed selective reaction monitoring (SRM) mode.

New object recognition (NOR) test. The number of mice exploring objects A (habituated object) and B (New object) was counted, and the recognitive index RI was calculated according to the formula as follows: $RI = N_B / (N_A + N_B)$ (N_A and N_B refer to the number of times the mice explored A and B, respectively).

Locomotor activity test. The total distance (L) and motion trajectory before and after epilepsy induced by PTZ were monitored by camera and converted into images using software (Supermaze, Shanghai Xinruan Soft Information Technology Co., Ltd.).

Statistics and reproducibility

All data analyses were performed using Origin 8.5. Statistical significance was determined using two-tailed *t*-tests. Significant differences are marked as **p* < 0.05, ***p* < 0.01, and ****p* < 0.001. All data are presented as mean ± SD. Sample sizes were chosen based on commonly accepted standards in the field and were sufficient to observe statistically meaningful differences. No data were excluded from the analysis unless explicitly stated, and the criteria for any exclusions are described in the corresponding figure legends. Randomization and blinding were not used unless otherwise indicated, as the experimental design focused on mechanistic investigations with clearly defined sample groups.

Reporting summary

Further information on research design is available in the Nature Portfolio Reporting Summary linked to this article.

Data availability

The data that support the findings of the study are included in the main text and supplementary information files. Source data are provided with this paper.

References

- Rabinowitch, I., Colón-Ramos, D. A. & Krieg, M. Understanding neural circuit function through synaptic engineering. *Nat. Rev. Neurosci.* **25**, 131–139 (2024).
- Wise, R. A. Dopamine, learning and motivation. *Nat. Rev. Neurosci.* **5**, 483–494 (2004).
- Pidathala, S. et al. Mechanisms of neurotransmitter transport and drug inhibition in human VMAT2. *Nature* **623**, 1086–1092 (2023).
- Cohen, J. Y. Dopamine and serotonin signals for reward across time scales. *Science* **350**, 47–48 (2015).
- Doty, R. L. Olfactory dysfunction in neurodegenerative diseases: is there a common pathological substrate? *Lancet Neurol.* **16**, 478–488 (2017).
- Russo, S. J. & Nestler, E. J. The brain reward circuitry in mood disorders. *Nat. Rev. Neurosci.* **14**, 609–625 (2013).
- Dahl, M. J., Mather, M. & Werkle-Bergner, M. Noradrenergic modulation of rhythmic neural activity shapes selective attention. *Trends Cogn. Sci.* **26**, 38–52 (2022).
- Kandel, E. R., Koester, J. D., Mack, S. H. & Siegelbaum, S. A. *Principles of Neural Science* 6th edn (McGraw-Hill, 2021).
- Berridge, K. C. The debate over dopamine's role in reward: the case for incentive salience. *Psychopharmacology* **191**, 391–431 (2007).
- Flames, N. & Hobert, O. Transcriptional control of the terminal fate of monoaminergic neurons. *Annu. Rev. Neurosci.* **34**, 153–184 (2011).
- Roeder, T. Octopamine in invertebrates. *Prog. Neurobiol.* **59**, 533–561 (1999).
- Joh, T. H. & Hwang, O. Dopamine beta-hydroxylase: biochemistry and molecular biology. *Ann. N. Y. Acad. Sci.* **493**, 342–350 (1987).
- Tao, Y. et al. Generation of locus coeruleus norepinephrine neurons from human pluripotent stem cells. *Nat. Biotechnol.* **42**, 1404–1416 (2023).
- Robertson, S. D., Plummer, N. W., de Marchena, J. & Jensen, P. Developmental origins of central norepinephrine neuron diversity. *Nat. Neurosci.* **16**, 1016–1023 (2013).
- Dunn, M. et al. Designing a norepinephrine optical tracer for imaging individual noradrenergic synapses and their activity in vivo. *Nat. Commun.* **9**, 2838 (2018).
- Day, J. C., Kornecook, T. J. & Quirion, R. Application of in vivo microdialysis to the study of cholinergic systems. *Methods* **23**, 21–39 (2001).
- Mingote, S., de Bruin, J. P. & Feenstra, M. G. Noradrenaline and dopamine efflux in the prefrontal cortex in relation to appetitive classical conditioning. *J. Neurosci.* **24**, 2475–2480 (2004).
- Sun, F. et al. A genetically encoded fluorescent sensor enables rapid and specific detection of dopamine in flies, fish, and mice. *Cell* **174**, 481–496 (2018).
- Kagiampaki, Z. et al. Sensitive multicolor indicators for monitoring norepinephrine in vivo. *Nat. Methods* **20**, 1426–1436 (2023).
- Feng, J. et al. A genetically encoded fluorescent sensor for rapid and specific in vivo detection of norepinephrine. *Neuron* **102**, 745–761 (2019).
- Zhou, N., Huo, F., Yue, Y. & Yin, C. Specific fluorescent probe based on “protect-deprotect” to visualize the norepinephrine signaling pathway and drug intervention tracers. *J. Am. Chem. Soc.* **142**, 17751–17755 (2020).
- Han, Y., Mao, L., Zhang, Q.-W. & Tian, Y. Sub-100 ms level ultrafast detection and near-infrared ratiometric fluorescence imaging of norepinephrine in live neurons and brains. *J. Am. Chem. Soc.* **145**, 23832–23841 (2023).
- Mao, L., Han, Y., Zhang, Q.-W. & Tian, Y. Two-photon fluorescence imaging and specifically biosensing of norepinephrine on a 100-ms timescale. *Nat. Commun.* **14**, 1419 (2023).
- Li, J. et al. A tissue-like neurotransmitter sensor for the brain and gut. *Nature* **606**, 94–101 (2022).
- Liu, Y., Liu, Z. & Tian, Y. Real-time tracking of electrical signals and an accurate quantification of chemical signals with long-term stability in the live brain. *Acc. Chem. Res.* **55**, 2821–2832 (2022).
- Muller, A., Joseph, V., Slesinger, P. A. & Kleinfeld, D. Cell-based reporters reveal in vivo dynamics of dopamine and norepinephrine release in murine cortex. *Nat. Methods* **11**, 1245 (2014).

27. Ye, X. et al. FRET modulated signaling: a versatile strategy to construct photoelectrochemical microsensors for in vivo analysis. *Angew. Chem. Int. Ed.* **60**, 11774–11778 (2021).
28. Zhao, Y., Wu, W., Fu, B., Gan, L. & Zhang, Z. Rationally design of near infrared light responsive micro-photoelectrodes for in vivo sensing of neurotransmitter molecules in mouse brain. *Chin. J. Chem.* **38**, 275–281 (2020).
29. Fu, B. & Zhang, Z. Rationally engineered photonic-plasmonic synergistic resonators in second near-infrared window for in vivo photoelectrochemical biodetection. *Nano Lett.* **19**, 9069–9074 (2019).
30. Wang, A., Li, J. & Zhang, T. Heterogeneous single-atom catalysis. *Nat. Rev. Chem.* **2**, 65–81 (2018).
31. Wu, W. & Zhang, Z. Defect-engineered TiO₂ nanotube photonic crystals for the fabrication of near-infrared photoelectrochemical sensor. *J. Mater. Chem. B* **5**, 4883–4889 (2017).
32. He, W. et al. Structural evolution of anatase-supported platinum nanoclusters into a platinum-titanium intermetallic containing platinum single atoms for enhanced catalytic CO oxidation. *Angew. Chem. Int. Ed.* **62**, e202213365 (2023).
33. Younan, S. M. et al. Zinc single atom confinement effects on catalysis in 1T-phase molybdenum disulfide. *ACS Nano* **17**, 1414–1426 (2023).
34. Henjum, K. et al. Cerebrospinal fluid catecholamines in delirium and dementia. *Brain Commun.* **3**, fcab121 (2021).
35. Lu, Z. et al. Bioinspired polynorepinephrine nanoparticles as an efficient vehicle for enhanced drug delivery. *J. Mater. Chem. B* **8**, 961–968 (2020).
36. Li, L. et al. Modulation of active center distance of hybrid perovskite for boosting photocatalytic reduction of carbon dioxide to ethylene. *Proc. Natl. Acad. Sci. USA* **121**, e2318970121 (2024).
37. Dong, Y., Xu, C. & Zhang, L. Construction of 3D Bi/ZnSnO₃ hollow microspheres for label-free highly selective photoelectrochemical recognition of norepinephrine. *Nanoscale* **13**, 9270–9279 (2021).
38. Lu, S., Fu, B. & Zhang, Z. Zwitterionic polymers coating anti-biofouling photoelectrochemical aptasensor for in vivo antibiotic metabolism monitoring and tracking. *Anal. Chem.* **94**, 14509–14516 (2022).
39. Rochford, A. E. et al. Functional neurological restoration of amputated peripheral nerve using biohybrid regenerative bioelectronics. *Sci. Adv.* **9**, eadd8162 (2023).
40. Zerbí, V. et al. Rapid reconfiguration of the functional connectome after chemogenetic locus coeruleus activation. *Neuron* **103**, 702–718 (2019).
41. Sun, Y., Hunt, S. & Sah, P. Norepinephrine and corticotropin-releasing hormone: partners in the neural circuits that underpin stress and anxiety. *Neuron* **87**, 468–470 (2015).
42. Dinunno, F. A., Dietz, N. M. & Joyner, M. J. Aging and forearm postjunctional α -adrenergic vasoconstriction in healthy men. *Circulation* **106**, 1349–1354 (2002).
43. Borchert, R. J. et al. Atomoxetine and citalopram alter brain network organization in Parkinson's disease. *Brain* **1**, 2632–1297 (2019).
44. González, H. F. J., Yengo-Kahn, A. & Englot, D. J. Vagus nerve stimulation for the treatment of epilepsy. *Lancet Neurol.* **30**, 219–230 (2019).
45. McKinney, R. A., Debanne, D., Gähwiler, B. H. & Thompson, S. M. Lesion-induced axonal sprouting and hyperexcitability in the hippocampus in vitro: implications for the genesis of posttraumatic epilepsy. *Nat. Med.* **3**, 990–996 (1997).
46. Yosefzon, Y. et al. Caspase-3 regulates YAP-dependent cell proliferation and organ size. *Mol. Cell* **70**, 573–587 (2018).

Acknowledgements

This research was supported by the National Natural Science Foundation of China (No. 22474041) (Z.Z.).

Author contributions

S.G. and Z.Z. designed the experiments. S.G. and J.H. carried out the synthesis of the photoelectrode and photoelectrochemical measurements. X.Z. and Y.L. performed the morphological and elemental characterizations. D.X. performed the DFT calculations. All authors wrote the manuscript.

Competing interests

The authors declare no competing interests.

Additional information

Supplementary information The online version contains supplementary material available at <https://doi.org/10.1038/s41467-025-60148-y>.

Correspondence and requests for materials should be addressed to Zhonghai Zhang.

Peer review information *Nature Communications* thanks Francesco Fornai and the other anonymous reviewer(s) for their contribution to the peer review of this work. A peer review file is available.

Reprints and permissions information is available at <http://www.nature.com/reprints>

Publisher's note Springer Nature remains neutral with regard to jurisdictional claims in published maps and institutional affiliations.

Open Access This article is licensed under a Creative Commons Attribution-NonCommercial-NoDerivatives 4.0 International License, which permits any non-commercial use, sharing, distribution and reproduction in any medium or format, as long as you give appropriate credit to the original author(s) and the source, provide a link to the Creative Commons licence, and indicate if you modified the licensed material. You do not have permission under this licence to share adapted material derived from this article or parts of it. The images or other third party material in this article are included in the article's Creative Commons licence, unless indicated otherwise in a credit line to the material. If material is not included in the article's Creative Commons licence and your intended use is not permitted by statutory regulation or exceeds the permitted use, you will need to obtain permission directly from the copyright holder. To view a copy of this licence, visit <http://creativecommons.org/licenses/by-nc-nd/4.0/>.

© The Author(s) 2025